System Modeling and Control of a Heliogyro Solar Sail

Adonis Pimienta-Peñalver*

University at Buffalo, State University of New York, Amherst, NY 14260

Liwei Tsai†

Iowa State University, Ames, IA 50011

Jer-Nan Juang‡

National Cheng Kung University, Tainan, Taiwan

John L. Crassidis§

University at Buffalo, State University of New York, Amherst, NY 14260

A heliogyro solar sail concept has recently been proposed as an alternative to deep space missions without the need for on-board propellant. Although this type of solar sail has existed conceptually for several decades, and some previous studies have investigated certain aspects of its operation, a significant amount of research is still needed to analyze the dynamic and control characteristics of the structure under the projected range of orbital conditions. This research effort provides an improvement upon the existing discrete-mass models of the heliogyro blade, and the extension of its application from a single membrane blade to a fully-coupled approximation of the dynamics of the structure with multiple spinning membrane blades around a central hub. Additionally, this work investigates the implementation of a control algorithm at each blade root to impose structural integrity and attitude control by coordinating well-known helicopter blade pitching profiles.

Introduction

Recent research has renewed interest in solar sailing technology to provide an alternative to undertake long-duration missions that would normally require a large amount of propellant. Of all the possible types of solar sail configurations, the heliogyro has the most understood control strategy and is the easiest to deploy [1]. The heliogyro design, which resembles a dutch windmill, was first introduced by Richard MacNeal in 1967 [2]. It makes use of long, thin, flexible blades that rotate about a central spacecraft hub in order to harness solar radiation pressure (SRP). This concept reduces the structural mass per area ratio, as it does away with spars and relies on centrifugal forces to stiffen the blade elements in rotation. As a consequence of their flexibility and size, heliogyro sails require persistent control attention in order to maintain stability. Precisely, the research effort presented in this paper is part of an on-going project, named 'HELIOS', at NASA Langley Research Center, which intends to investigate the instrumentation and control architecture necessary to maneuver the blades of a heliogyro vehicle. The practical impediments of maintaining such a large structure for testing on Earth has historically led researchers to carry out purely simulation-based work, or conduct experiments on scaled models; this is why further work must be carried out to demonstrate the practicality of a heliogyro concept demonstration mission.

A common denominator among previous control research on heliogyros is the conclusion that the controllers must be driven toward models that capture more of the dynamic characteristics of the flexible blades. To summarize, the three most common techniques to model heliogyro blade dynamics include analytical, discretizing, and finite element methods. Analytical methods produce fully-coupled continuous beam equations, which must be solved using numerical techniques, incurring considerable computational loads [3–6]. Discretizing methods tradeoff some fidelity for ease of computation, approximating the flexible sails through

*Graduate Student, Department of Mechanical & Aerospace Engineering. arp27@buffalo.edu.

†Graduate Student, Department of Aerospace Engineering. liwei@iastate.edu.

‡Honorary Professor. Department of Engineering Science. jjuang88@gmail.com. Fellow AIAA.

§CUBRC Professor in Space Situational Awareness. Department of Mechanical & Aerospace Engineering. johnc@buffalo.edu. Fellow AIAA.

some lumping of the total mass in a deliberate pattern [7–10]. Finally, finite element methods require the use of dedicated FEA software, which give rise to high computational demands [11]. The present study improves the computationally-friendly discretized models with the fidelity of distributed parameter approaches by incorporating structural stiffness properties onto the lumped-mass approximations of the blade. Initial work along this vein has already been carried out in Ref. [12], where the stability of a single blade –and thus, flutter– is investigated at differing levels of SRP and spin rates. As a prolongation of the work in Ref. [9], the present investigation also employs a hybrid-coordinate approach, following Meirovitch's formulation [13], to represent the full heliogyro by adding a continuous hub to the discretized blades. Further analysis is performed in [14], where the approach is extended to heliogyros with multiple blades.

The stability and attitude control in all six degrees of freedom of the heliogyro is achieved through the coordination of three pitching profiles commonly associated with helicopter rotor controls: collective, cyclic, and half-pitch from each of the blade roots, as seen in Figure 1. Although it has been demonstrated

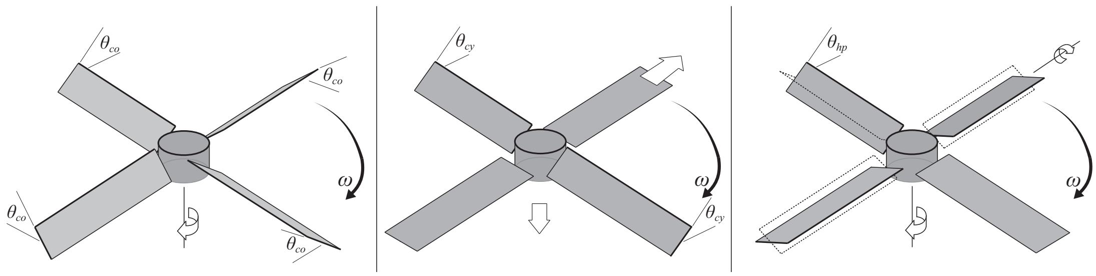

Figure 1: Collective, Cyclic, and Half-Pitch Maneuvers

that it is always theoretically possible to change the orientation of a heliogyro, even when it is edge on to the Sun, previous literature has circumvented the command-lag issues associated with gossamer sails by assuming, for example, that the blade is completely flat, or that stiffening agents are in place to guarantee blade uniformity. With the aim to address these issues, this paper presents a simulation-based study of the approximate structural dynamics of the full heliogyro structure under the effects of SRP and control command, the latter of which consists of actuating motors at the blade roots to change blade pitching which, in turn, affect the structure's orientation. This work demonstrates the chosen predictive control algorithm as a viable method to impose regulation and maneuver tracking through pertinent simulations.

Attitude System

The size and gossamer nature of the heliogyro structure has historically made it difficult to study the system on Earth. Researchers have therefore resorted to methods such as closed-form solutions, discretizations, and FEA, which are usually either too simplistic, or too computationally complex. This section introduces a lumped-mass method which describes coupling among all system coordinates and accounts for aeroelasticity effects in a straightforward, repeatable procedure. In this paper, the modeling approach consists of dividing the blade into equal sections, where the total mass is proportionally lumped into discrete points located at the edges of these sections; the point masses are separated from each other by massless, but rigid rods. The hub of the heliogyro is shaped as a thick disk of mass m_h, radius r_h and thickness h, as shown in Figure 2.

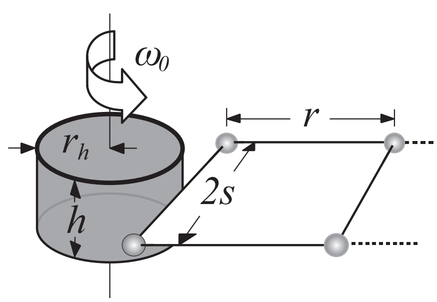

Figure 2: Hybrid Model: Continuous Hub and Discrete Masses (1-blade + hub)

Position & Velocity Formulation

Three fundamental motions have been defined to describe the vibration of each blade segment, all of which are constrained by the distance of the massless rods. These include the angular measures of out-of-plane bending, twisting, and in-plane bending. For the sake of better representing stress-strain relations within the blade system, these angular motions are redefined as linear coordinates and conformed into the rigidity of the lumped-mass model. As seen in Figure 3, the coordinates consist of axial (u, v, and w, for the x, y, and z directions, respectively) and torsional (φ) elastic deformations due to stress and strain.

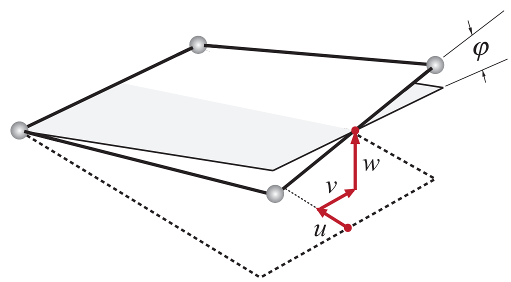

Figure 3: Deformations

Thus, the generalized coordinates are collected in the following:

$$\mathbf{q} = [w_{ji}\, v_{ji}\, \varphi_{ji}\, ...]^T \quad \text{for} \quad \begin{matrix} j \in \{1 \rightarrow n_b\} \\ i \in \{1 \rightarrow n_s\} \end{matrix} \tag{1}$$

The axial deformation, u, is ignored entirely in this definition because, as it turns out, it can be defined entirely in terms of w, v and r. Note that n_b and n_s refer to the number of blades in the heliogyro, and the number of segments per blade, respectively.

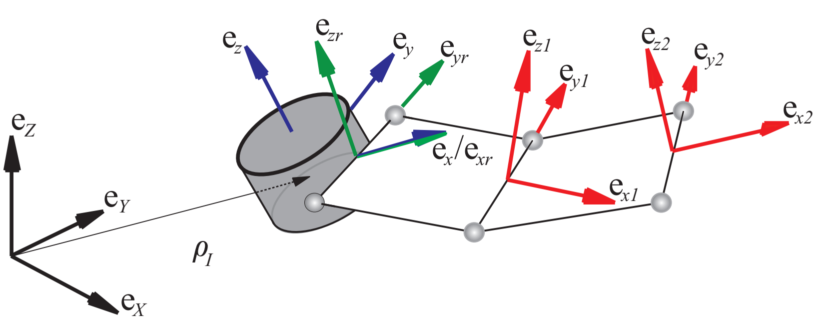

Figure 4: Blade (red), Root (green), Hub –Body– (blue), and Inertial (black) Frames

Figure 4 shows the coordinate systems utilized hereafter: the segment-fixed blade coordinate systems for each section ($[\mathbf{e}_{xi}, \mathbf{e}_{yi}, \mathbf{e}_{zi}] \in \mathcal{B}$, in red), the root frame ($[\mathbf{e}_{xr}, \mathbf{e}_{yr}, \mathbf{e}_{zr}] \in \mathcal{R}$, in green) which is fixed to the actuator, the body-fixed hub coordinate system ($[\mathbf{e}_{x}, \mathbf{e}_{y}, \mathbf{e}_{z}] \in \mathcal{H}$, in blue), as well as some inertial manifold ($[\mathbf{e}_{X}, \mathbf{e}_{Y}, \mathbf{e}_{Z}] \in \mathcal{I}$, in black).

For the conversion between the blade, $\mathcal{B}$, and the root, $\mathcal{R}$, frames, it is desirable to express the out-of-plane and the in-plane bending angles in terms of the generalized coordinates of Eq. (1). A 1-2-3 Euler rotation sequence is followed, which begins with the twisting, then out-of-plane, then in-plane bending. The transcendental equations (cosines and sines) operating on the bending angles are converted into expressions carrying only the deflection coordinates in Eq. (1). Thus, the transformation carried out by $T_{\mathcal{RB}i}$, from the ith blade frame, $\mathcal{B}$, to the root frame, $\mathcal{R}$, in terms of the generalized system coordinates is given by

$$T_{\mathcal{RB}} = \begin{bmatrix} 1 & 0 & 0 \\ 0 & \cos\varphi_i & \sin\varphi_i \\ 0 & -\sin\varphi_i & \cos\varphi_i \end{bmatrix} \begin{bmatrix} \frac{\sqrt{r^2-w_i^2}}{r} & 0 & \frac{w_i}{r} \\ 0 & 1 & 0 \\ -\frac{w_i}{r} & 0 & \frac{\sqrt{r^2-w_i^2}}{r} \end{bmatrix} \begin{bmatrix} \frac{\sqrt{r^2-w_i^2-v_i^2}}{\sqrt{r^2-w_i^2}} & \frac{v_i}{\sqrt{r^2-w_i^2}} & 0 \\ -\frac{v_i}{\sqrt{r^2-w_i^2}} & \frac{\sqrt{r^2-w_i^2-v_i^2}}{\sqrt{r^2-w_i^2}} & 0 \\ 0 & 0 & 1 \end{bmatrix} \tag{2}$$

Note that this also serves as the transformations form the ith to the (i-1)th blade frames. The transformation from the root frame $\mathcal{R}$ to the hub frame $\mathcal{H}$ is carried out by $T_{\mathcal{HR}i}$ using the following conversion:

$$T_{\mathcal{HR}i} = \begin{bmatrix} 1 & 0 & 0 \\ 0 & \cos\theta & -\sin\theta \\ 0 & \sin\theta & \cos\theta \end{bmatrix} \tag{3}$$

Note that the root, $\mathcal{R}$, frame and the hub, $\mathcal{H}$, frame both share the same x-direction (see Figure 4); the pitching angle θ will be the only manner in which control command can be transferred onto the blade. These transformations are necessary to resolve the expression for the position of a tip mass, which is given as

$$\mathbf{R}_i = \begin{bmatrix} \rho_X \\ \rho_Y \\ \rho_Z \end{bmatrix}_{\mathcal{I}} + T_{\mathcal{HR}} T_{\mathcal{RB}i} \begin{bmatrix} r \\ s \\ 0 \end{bmatrix}_{\mathcal{B}} + \mathbf{R}_{(i-1)\mathcal{H}} \quad \text{for } i \in \{1 \rightarrow n_s\}, \text{ where } \mathbf{R}_0 = T_{\mathcal{HR}} \begin{bmatrix} r_h \\ s \\ 0 \end{bmatrix}_{\mathcal{R}} \tag{4}$$

For multiple blade sections, this becomes an additive process where all segment components are added together from tip to root. With the lumped-mass positions defined in terms of the chosen coordinate system, it becomes straightforward to derive the velocity expressions which are necessary to account for the kinetic energies of the system. The following 3-2-1 sequence carries out the conversion from the hub frame, $\mathcal{H}$, to the inertial frame, $\mathcal{I}$; which is chosen to better represent the rotation o_3 about the spin axis

$$T_{\mathcal{IH}} = \begin{bmatrix} 1 & 0 & 0 \\ 0 & \cos o_1 & \sin o_1 \\ 0 & -\sin o_1 & \cos o_1 \end{bmatrix} \begin{bmatrix} \cos o_2 & 0 & -\sin o_2 \\ 0 & 1 & 0 \\ \sin o_2 & 0 & \cos o_2 \end{bmatrix} \begin{bmatrix} \cos o_3 & \sin o_3 & 0 \\ -\sin o_3 & \cos o_3 & 0 \\ 0 & 0 & 1 \end{bmatrix} \tag{5}$$

The expressions of velocity, which are not shown here for the sake of space, can then be completely defined in terms of the generalized coordinates of the system (Eq. (1)), the Euler angles (o_1, o_2, and o_3), and the body rates (ω_x, ω_y, and ω_z).

Energy Terms / Lagrangian Approach

The kinetic and potential energies for the attitude dynamics of the lumped-mass system are given in the following relations:

$$T = \frac{1}{2} m \left(\sum_{i=1}^{n} \left(\dot{\mathbf{R}}_{i\mathcal{B}} \cdot \dot{\mathbf{R}}_{i\mathcal{B}} \right) \right) + \frac{1}{2} \left(I_{xx}\omega_x^2 + I_{yy}\omega_y^2 + I_{zz}\omega_z^2 \right) \tag{6}$$

$$V = \sum_{i=0}^{n} \left(\int_{-s}^{s} \left(\frac{1}{2} E\epsilon_{ixx}^2 + \frac{1}{2} G\epsilon_{ixy}^2 + \frac{1}{2} G\epsilon_{ixz}^2 \right) dy \right) \tag{7}$$

where the quantities E, and G, are the stress and shear modules, respectively; also, ϵ_{xx} represents the axial strain, while ϵ_{xy} and ϵ_{xz} represent the shear strain along the out-of-plane direction.

In order to continue with the development of the equations of motion, it is imperative that both the expressions of energy are given in terms of the system generalized coordinates (Eq. 1) and additional known parameters such as mass, or size, etc. This is true for the kinetic energy expression but, for the potential energy, it is necessary to find a way to cast the strain variables, ϵ_{xx}, ϵ_{xy}, and ϵ_{xz}, into functions of the generalized coordinates, as well. Reference [3] derives the aforementioned strain deformations for a continuous rotor blade, these quanities are then assimilated to the discretized system of the heliogyro blade. The underlying hypothesis of this interpretation is that the same set of strain-displacement relationships may be used on the heliogyro blade if it is imagined as special case of a rotor blade; that is, a rotor blade with minimal thickness.

The corresponding relative displacements on the e_{xi}, e_{yi}, and e_{zi} directions are defined as $\bar{u}$, $\bar{v}$, and $\bar{w}$, respectively. Additionally, $\bar{\phi}$ corresponds to the total angle of twist along the elastic axis (e_{xi}). Equation (8) shows how these quantities are obtained from the present model. Note that, since we assume symmetry about the elastic axis (e_{xi}), the point masses along either edge of the discretized blade may be used for the following definitions:

$$
\begin{aligned}
\bar{w}_i &= \mathbf{R}_{i\mathcal{H}z}\big|_{s=0} \\
\bar{v}_i &= \mathbf{R}_{i\mathcal{H}y}\big|_{s=0} \\
\bar{u}_i &= \mathbf{R}_{i\mathcal{H}x}\big|_{s=0} - r\cdot i \\
\bar{\phi}_i &= \textstyle\sum_{k=1}^{i}\varphi_k
\end{aligned}
\quad \text{with} \quad
\begin{aligned}
\bar{w}_0 &= 0 & \bar{v}_0 &= 0 \\
\bar{w}_0' &= 0 & \bar{v}_0' &= 0 \\
\bar{w}_n'' &= 0 & \bar{v}_n'' &= 0
\end{aligned}
\quad
\begin{aligned}
\bar{\phi}_0 &= 0 \\
\bar{\phi}_n' &= 0
\end{aligned}
\tag{8}
$$

Forward and backward finite difference approximations are used to formulate the spatial derivatives of these quantities:

$$
\begin{aligned}
\bar{w}_i' &= \frac{\bar{w}_i - \bar{w}_{i-1}}{r}, & \bar{w}_i'' &= \frac{\bar{w}_i' - \bar{w}_{i-1}'}{r} \\
\bar{v}_i' &= \frac{\bar{v}_i - \bar{v}_{i-1}}{r}, & \bar{v}_i'' &= \frac{\bar{v}_i' - \bar{v}_{i-1}'}{r} \\
\bar{u}_i' &= \frac{\bar{u}_i - \bar{u}_{i-1}}{r}, & \bar{\phi}_i' &= \frac{\bar{\phi}_{i+1} - \bar{\phi}_i}{r}
\end{aligned}
\tag{9}
$$

If the heliogyro membrane blade is imagined as a very thin rotor blade, the elastic strain-displacement relations found in Ref. [3] may be put to use. The strains on the blade are thus approximated as

$$
\begin{aligned}
\epsilon_{ixx} &= \bar{u}_i' + \frac{\bar{v}_i'^2}{2} + \frac{\bar{w}_i'^2}{2} + y^2\frac{\bar{\phi}_i'^2}{2} - \bar{v}_i''\left(y\cos\left(\bar{\phi}_i+\theta\right)\right) - \bar{w}_i''\left(y\sin\left(\bar{\phi}_i+\theta\right)\right) \\
\epsilon_{ixy} &= y\bar{\phi}_i' \\
\epsilon_{ixz} &= 0
\end{aligned}
\tag{10}
$$

where the variable y represents an arbitrary position along the blade cross section. Note that the terms corresponding to the out-of-plane direction, which produced relations associated with the thickness of the blade, are neglected in this approximation due to the extremely thin nature of a heliogyro membrane blade.

An unintended consequence of the approximating procedure is that, as the physical system is discretized into lumped masses, then an appropriate discretization of the stress and shear moduli, E and G, is also necessary. This is one of the major challenges of this study, and some work is still needed to normalize this process.

Following the Lagrangian approach ($L = T - V$), the EOMs that describe the fully-coupled nonlinear blade behavior may be obtained using the common relation:

$$
\frac{d}{dt}\left(\frac{\partial L}{\partial \dot{\mathbf{q}}_i}\right) - \frac{\partial L}{\partial \mathbf{q}_i} = \tau_{\mathbf{q}_i}, \qquad \text{where} \quad \mathbf{q} = \begin{bmatrix} w_i \\ v_i \\ \varphi_i \end{bmatrix}
\tag{11}
$$

while the corresponding form of Lagrange's equation that describes the attitude dynamics of the system in terms of quasi-coordinates is given by

$$
\frac{d}{dt}\left(\frac{\partial L}{\partial \omega_l}\right) - [\Omega\times]\frac{\partial L}{\partial \omega_l} - B^T\frac{\partial L}{\partial o_l} = B^T\tau_{o_l}, \quad \text{where} \quad l \begin{cases} \in \{x,y,z\} & \text{for} \quad \omega \\ \in \{1,2,3\} & \text{for} \quad o \end{cases}
\tag{12}
$$

In Eq. (12), the body angular rates ω_x, ω_y, and ω_z are utilized in place of the generalized coordinates $\dot{o}_1$, $\dot{o}_2$, and $\dot{o}_3$. This development follows the derivation of Ref. [13], and is done for the sake of convenience, as it is easier to formulate the kinetic energy, as well as any form of feedback control law, based on angular velocities about orthogonal body axes x, y, and z; as opposed to a formulation based on the Euler angles o_1, o_2, and o_3.

In Eqs. (11) and (12), the torques applied onto each of the generalized coordinates, including the body rates, are given by τ_{q_i} and τ_{o_l}. According to mission specifications, τ_{q_i} would correspond with pitching torque inputs at the root of the blade, and τ_{o_l} would equate to magnetic torquer inputs at the hub, which are expected to aid in the de-tumbling process before sail deployment, or attitude changing moments induced by coordinated pitching from the blades. Furthermore, $[\Omega\times]$ represents the cross-product matrix of the body rates (ω_x, ω_y, and ω_z). The quantity B stands for the kinematic matrix associated with the particular Euler angle rotation utilized to convert from the hub (body) frame to the inertial frame (Eq. (5)).

The inversion of the kinematic matrix, B, from a 3-2-1 rotation, shows that, for small Euler angles o_1 and o_2, the quasi-coordinate angular rates may be approximated as the Euler angle rates:

$$\begin{bmatrix}\omega_x\\ \omega_y\\ \omega_z\end{bmatrix} = \begin{bmatrix}-\sin o_2 & 0 & 1\\ \cos o_2 \sin o_1 & \cos o_1 & 0\\ \cos o_2 \cos o_1 & -\sin o_1 & 0\end{bmatrix}\begin{bmatrix}\dot{o}_3\\ \dot{o}_2\\ \dot{o}_1\end{bmatrix}$$
$$\text{If} \quad o_2, o_1 \ll 1, \quad \text{then} \quad \begin{matrix}\omega_x \approx \dot{o}_1\\ \omega_y \approx \dot{o}_2\\ \omega_z \approx \dot{o}_3\end{matrix} \tag{13}$$

This is convenient when linearizing the system, because it allows to interpret the body rates ω_x, ω_y, and ω_z, as the derivatives of the Euler angles, which in turn allows to configure the system's state vector to reflect this equivalence when a linearization is applied.

SRP Forcing

In this paper, a very simple model of the effect of the SRP on each blade segment is set to only consider the specular component of the reflection, while secondary effects, such as albedo or self-illumination are ignored.

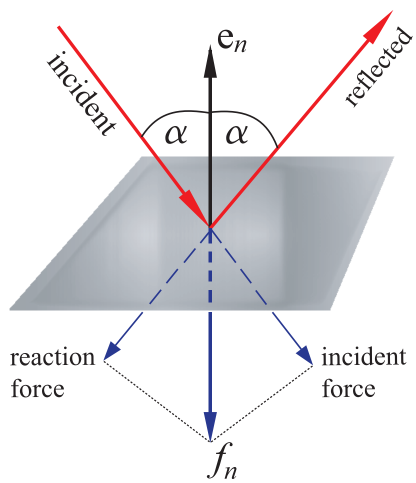

Figure 5: Forces Exerted and Produced on a Perfectly Reflecting Surface Under SRP

If a perfect reflector is assumed, the total forcing contribution from SRP will be a composition of both the incident force from the incoming light, and the reaction force from the reflected photons. Hence, the following equality is used to approximate the SRP influence along the normal for each segment

$$\mathbf{f}_n = -f_{\text{srp}}\left(\cos^2\alpha\right)\mathbf{e}_n = -f_{\text{srp}}\left(\mathbf{e}_i \cdot \mathbf{e}_n\right)^2\mathbf{e}_n \tag{14}$$

where $\mathbf{e}_i$ is the incident unit vector, $\mathbf{e}_n$ is the unit normal at an arbitrary point on the segment surface, and α represents the inscribed half angle. In the discrete-mass model, the SRP is assumed to be equally distributed on each of the point masses, yielding the following external torque vector with respect to each generalized coordinate, which is found by applying the principle of virtual work:

$$\tau_q = \sum_{i=1}^{n_s}\left(\mathbf{f}_{ni} \cdot \frac{\delta\mathbf{R1}}{\delta\mathbf{q}} + \mathbf{f}_{ni} \cdot \frac{\delta\mathbf{R2}}{\delta\mathbf{q}}\right) \tag{15}$$

where $\mathbf{R1}$ and $\mathbf{R2}$ are to the position of the point mass pairs to the extremes of each segment's chord.

To gain an understanding for the behavior of the heliogyro system, it is necessary to analyze its linearized form around coordinates of static deflection. Although these instances of equilibrium are not unique to any of the system's generalized coordinates, the modeling approach undertaken in this study assumes that the only non-negligible instance of static deflection occurs in the out-of-plane, w, direction of each segment. This is explained as follows: as the entire heliogyro structure spins up, the centrifugal force generated by the rotation will, at some point, reach equilibrium with the normal force that the SRP exerts on each blade. This state of static deflection is obtained by setting all displacement variables (other than out-of-plane bending) and derivatives to zero, equating the results to the constant terms of the SRP forcing, and solving for the permanent out-of-plane bending, w_s. The system is permitted to oscillate in the out-of-plane direction through the Δw coordinate. Linearizing the system around a constant rotation about the $\mathbf{e}_z$-axis in the body frame is set to follow a nominal rpm value, ω_0, around which variations, $\Delta\omega$, are allowed.

Dynamic Behavior

Table 1 shows relevant simulation parameters utilized in this paper and their equivalences in the HELIOS mission while Table 2 lists all the natural frequencies of the linearized system at 0 SRP based on the blade's spin rate, ω_0; these results agree with those obtained by MacNeal's original analytical model of ref. [4].

Table 1: Physical Parameters Used in the Simulation

HELIOS Parameters		Simulation Parameters	
Blade mass (M_b)	0.674 kg	No. of point masses	N
Blade length (R)	220 m	No. of segments (n_s)	$(N-2)/2$
Blade width	0.75 m	Point mass	M_b/N
Blade thickness	2.54×10^{-6} m	Segment length (r)	R/n_s
Blade density	1420 kg/m^3	Segment half-chord (s)	0.375 m

Table 2: Natural Frequencies of the Single Spinning Membrane

No. of segments	Mode	Frequency
1	in-plane	0
	out-of-plane	ω_0
	twisting	$\omega_0\sqrt{2}$
2	in-plane	$0,\ \omega_0\sqrt{5}$
	out-of-plane	$\omega_0,\ \omega_0\sqrt{6}$
	twisting	$\omega_0\sqrt{2},\ \omega_0\sqrt{7}$
3	in-plane	$0,\ \omega_0\sqrt{5},\ \omega_0\sqrt{14}$
	out-of-plane	$\omega_0,\ \omega_0\sqrt{6},\ \omega_0\sqrt{15}$
	twisting	$\omega_0\sqrt{2},\ \omega_0\sqrt{7},\ \omega_0\sqrt{16}$
MacNeal's	in-plane	$\omega\sqrt{\frac{n(n+1)}{2}-1},\ n=1,3,5...$
	out-of-plane	$\omega\sqrt{\frac{n(n+1)}{2}},\ n=1,3,5...$
	twisting	$\omega\sqrt{\frac{n(n+1)}{2}+1},\ n=1,3,5...$

Figure 6 shows results for increasing n_s from 1 to 5 segments, where the successive approximations are evidently approaching onto one definitive out-of-plane static deflection curve, which converges at about 0.88 m of flexing for the tip. The results of Figure 6, based on simulations at $\omega_0 = 0.6$ rpm and $11{\times}10^{-6}$ Pa of SRP, agree closely with the FEA results of Ref. [15], which predict a tip deflection of about 0.82 m at the same orbital conditions.

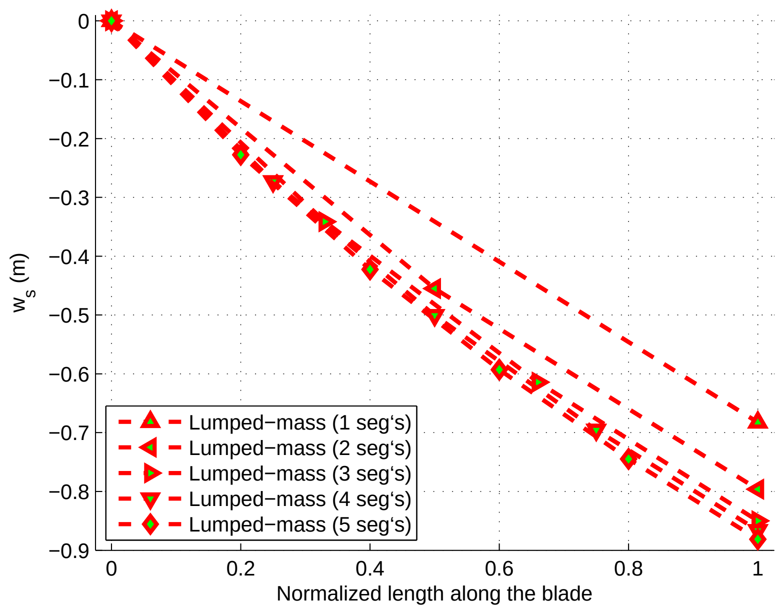

Figure 6: Normalized Blade Profile Under Static Deflection

The following studies consist of an inspection of the changing stability conditions of the heliogyro under differing amounts of SRP, which is, in other words, a study of the relation between structural stability and distance to the Sun. For the linearized system, the imaginary part of the eigenvalues are normalized by the nominal spinning rate of the structure and are then tracked as a function of incident SRP. Figure 7a is a simulation of the single blade system with five approximating segments at $\omega_0 = 0.55$ rpm. The instance of flutter (red curve), which correspond to a coalescence of the the first twisting and in-plane modes, occurs near $9.1{\times}10^{-6}$ Pa. At this point, the system's eigenvalues start to develop real parts, making the sail unstable. Although instabilities at higher levels of SRP are physically insignificant, it is worth noting that divergence (blue curve) is seen around the value of $21{\times}10^{-6}$ Pa where the corresponding eigenvalues become completely part of the real number set. The simulation in Figure 7a predicts that, in order avoid flutter near the Earth ($9.1{\times}10^{-6}$ Pa), the spinning rate has to surpass 0.55 rpm, which is close to the forecast of 0.645 rpm given by the continous model developed by NASA and NIA [15]. This slight discrepancy does not necessarily point toward the inaccuracy of the lumped-mass approach, given that NASA's model is also an approximation, and there is no operational data to calibrate against.

The normalized frequencies plot in Figure 7b shows that, at 1 rpm, instabilities occurs in separate instances as the blade's twisting frequencies (both symmetric and asymmetric modes) converge to the in-plane frequencies. The two twisting frequencies that start near 1.4 on the y-axis of the Figure and the two in-plane frequencies that immediately precede a ratio of 1, are both symmetric and antisymmetric modes of the twisting, and in-plane motions, respectively. To be specific, Figure 7b shows that the asymmetric modes converge near $43{\times}10^{-6}$ Pa, while the symmetric twisting and in-plane modes converge at a slightly higher level of SRP. This simulation, obtained with five segments per blade, approximates the results of the analytical model developed by NASA [15], for the asymmetric convergence. It should be noted that the symmetric in-plane mode in this model of the lumped mass approach is highly dominated by the hub's rotation about the $\mathbf{e}_z$-axis, which is something to be expected.

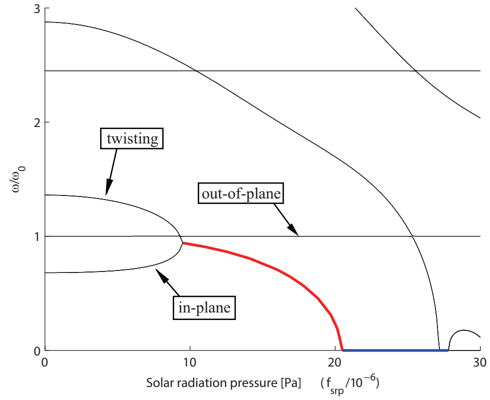

(a) Single Blade Normalized Freq., ω_0=0.55 rpm

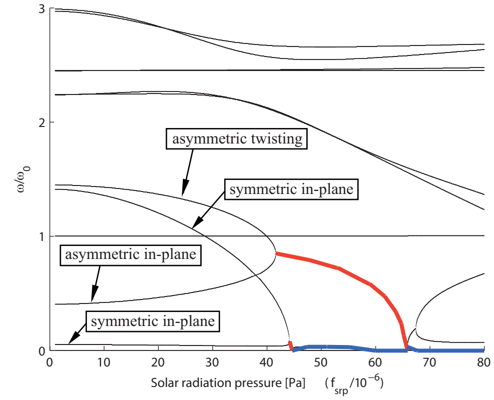

(b) Two Blade and Hub Normalized Freq., ω_0=1 rpm

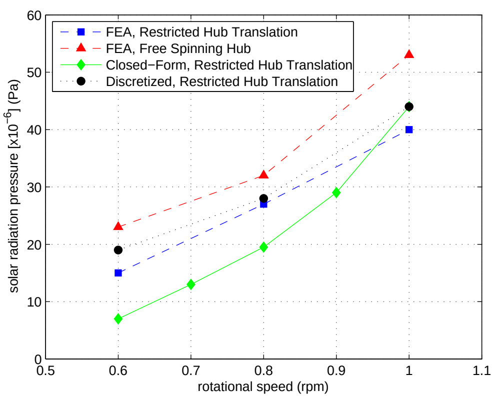

(c) Comparison of Flutter SRP with NASA Two-blade Models, Data Source: [15]

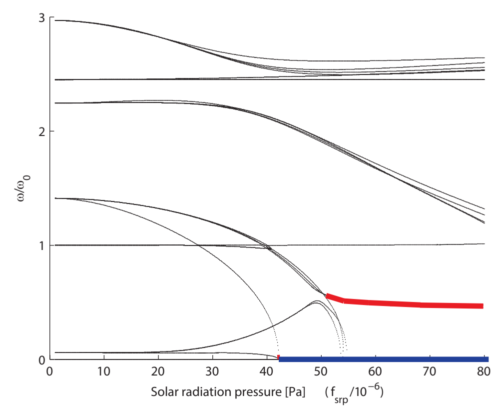

(d) Four Blade and Hub Normalized Freq.

Figure 7: Stability Results for Discretized Models

Figure 7c compares the simulation of Figure 7b with the solarelastic flutter point results from the closed-form analytical solution and the FEA approaches developed by NASA and NIA for the two-bladed heliogyro at a range of rpm levels. It is interesting to note that the solarelastic boundary predictions from the lumped mass approach seem to be more similar, or at least follow in trend, to those of the FEA models, only matching the predictions of the closed-form analytical model at the 1 rpm spin rate.

The four-bladed structure has an increased sail area to mass ratio, which theoretically enhances the control command capabilities for the attitude system. The normalized frequencies plot for the free spinning model in Figure 7d shows once again that, at 1 rpm, instabilities occurs in separate instances as the twisting frequencies of the blades converge into the in-plane modes of the system. The distinction of symmetric and antisymmetric convergence is still maintained in this system. However, it is evident that the increased mass agglomeration along the length of the $\mathbf{e}_y$ body axis has established the dominance of the hub's own rotations over the in-plane modes. The evidence from this and previous models suggests that this trend becomes even more prominent as the number of blades increases. Figure 7d shows that the asymmetric modes converge near 53×10^{-6} Pa, while the symmetric twisting and in-plane modes converge to a divergence instability near 42×10^{-6} Pa of SRP.

Generalized Predictive Control

The generalized predictive control (GPC) algorithm presented in this section makes use of multi-step-ahead output prediction based on the finite difference model. The system output predictions are cast over a set interval of future time known as *prediction horizon*, h_p, while the synthesized inputs are applied over an interval known as *control horizon*, h_c. These control inputs are derived from minimization of a cost function that takes into account measurement error and a control penalty term.

For a system with r_c control inputs, r_d disturbance inputs, n states, and m outputs, the finite difference model at time k is given by

$$\begin{aligned}\mathbf{y}(k) &+ \alpha_1\mathbf{y}(k-1) + \cdots + \alpha_p\mathbf{y}(k-p)\\ &= \beta_0\mathbf{u}(k) + \beta_1\mathbf{u}(k-1) + \cdots + \beta_p\mathbf{u}(k-p)\\ &+ \gamma_0\mathbf{d}(k) + \gamma_1\mathbf{d}(k-1) + \cdots + \gamma_p\mathbf{d}(k-p)\end{aligned} \tag{16}$$

where p is the ARX model order, $\mathbf{u}(k)$ is the $r_c \times 1$ control input vector, $\mathbf{d}(k)$ is the $r_d \times 1$ disturbance input vector, and $\mathbf{y}(k)$ is the $m \times 1$ output vector at time k. In Eq. (16), the coefficient matrices α_i and β_i, of sizes $m \times m$ and $m \times r_c$, respectively, for $i \in \{0 \to p\}$, are known as the observer Markov parameters. The matrices γ_i, of size $m \times r_d$ are the weighting terms for the disturbance inputs, which are assumed to be unknown, and thus modeled as Gaussian white noise, in this study.

When a system identification algorithm is used, such as those of Chapter 10 in Ref. [16], the ARX parameters, α_i and β_i, can be obtained from input and output data to form the $\mathcal{A}$ and $\mathcal{B}$ matrices. Specifically, the data matrices $\mathtt{Y}$ and $\mathtt{V}$ are made up of the collected I/O histories.

$$\begin{aligned}\mathtt{Y} &= \begin{bmatrix}\mathbf{y}(k-p) & \mathbf{y}(k-p+1) & \cdots & \mathbf{y}(k-1)\end{bmatrix}\\ \mathtt{V} &= \begin{bmatrix}\mathbf{u}(k-p) & \mathbf{u}(k-p+1) & \cdots & \mathbf{u}(k-1)\\ \mathbf{y}(k-p) & \mathbf{y}(k-p+1) & \cdots & \mathbf{y}(k-1)\\ \vdots & \vdots & \ddots & \vdots\\ \mathbf{u}(2) & \mathbf{u}(3) & \cdots & \mathbf{u}(k-p)\\ \mathbf{y}(1) & \mathbf{y}(2) & \cdots & \mathbf{y}(k-p)\end{bmatrix}\end{aligned} \tag{17}$$

Then, the ARX coefficients are given as

$$\mathtt{P} = \begin{bmatrix}\beta_1 & \alpha_1 & \beta_2 & \alpha_2 & \cdots & \beta_p & \alpha_p\end{bmatrix} = \mathtt{Y}\mathtt{V}^\dagger \tag{18}$$

where $()^\dagger$ denotes a pseudo-inverse operation.

A recursive technique is utilized to predict $\mathbf{y}_s(k)$, the future outputs:

$$\mathbf{y}_s(k) = \mathcal{T}\mathbf{u}_s(k) + \mathcal{B}\mathbf{u}_p(k-p) - \mathcal{A}\mathbf{y}_p(k-p) \tag{19}$$

where $\mathbf{y}_p(k-p)$ represents the vector of past outputs, $\mathbf{u}_s(k)$ and $\mathbf{u}_p(k-p)$ are the future and past input vectors, respectively, which are homologous to

$$\mathbf{y}_s(k) = \begin{bmatrix}\mathbf{y}(k)\\ \mathbf{y}(k+1)\\ \vdots\\ \mathbf{y}(k+s-1)\end{bmatrix} \qquad \mathbf{y}_p(k-p) = \begin{bmatrix}\mathbf{y}(k-p)\\ \mathbf{y}(k-p+1)\\ \vdots\\ \mathbf{y}(k-1)\end{bmatrix} \tag{20}$$

where the integer s represents the desired prediction horizon.

The matrices $\mathcal{T}$, $\mathcal{A}$, and $\mathcal{B}$, are given by the following matrices, where $\mathcal{T}$ is the systems toeplitz matrix formed from the ARX parameters.

$$\mathcal{T} = \begin{bmatrix}\beta_0 & & & \\ \beta_0^{(1)} & \beta_0 & & \\ \vdots & \vdots & \ddots & \\ \beta_0^{(s-1)} & \beta_0^{(s-2)} & \cdots & \beta_0\end{bmatrix} \tag{21}$$

$$\mathcal{A} = \begin{bmatrix}\alpha_p & \alpha_{(p-1)} & \cdots & \alpha_1\\ \alpha_p^{(1)} & \alpha_{(p-1)}^{(1)} & \cdots & \alpha_1^{(1)}\\ \vdots & \vdots & \ddots & \vdots\\ \alpha_p^{(s-1)} & \alpha_{(p-1)}^{(s-1)} & \cdots & \alpha_1^{(s-1)}\end{bmatrix} \qquad \mathcal{B} = \begin{bmatrix}\beta_p & \beta_{(p-1)} & \cdots & \beta_1\\ \beta_p^{(1)} & \beta_{(p-1)}^{(1)} & \cdots & \beta_1^{(1)}\\ \vdots & \vdots & \ddots & \vdots\\ \beta_p^{(s-1)} & \beta_{(p-1)}^{(s-1)} & \cdots & \beta_1^{(s-1)}\end{bmatrix} \tag{22}$$

The prediction ARX parameters are found from

$$
\begin{array}{ll}
\begin{aligned}
\alpha_1^{(j)} &= \alpha_2^{(j-1)} - \alpha_1^{(j-1)}\alpha_1 \\
\alpha_2^{(j)} &= \alpha_3^{(j-1)} - \alpha_1^{(j-1)}\alpha_2 \\
&\vdots \\
\alpha_{p-1}^{(j)} &= \alpha_p^{(j-1)} - \alpha_1^{(j-1)}\alpha_{p-1} \\
\alpha_p^{(j)} &= -\alpha_1^{(j-1)}\alpha_p
\end{aligned}
&
\begin{aligned}
\beta_0^{(j)} &= \beta_1^{(j-1)} - \alpha_1^{(j-1)}\beta_0 \\
\beta_1^{(j)} &= \beta_2^{(j-1)} - \alpha_1^{(j-1)}\beta_1 \\
\beta_2^{(j)} &= \beta_3^{(j-1)} - \alpha_1^{(j-1)}\beta_2 \\
&\vdots \\
\beta_{p-1}^{(j)} &= \beta_p^{(j-1)} - \alpha_1^{(j-1)}\beta_{p-1} \\
\beta_p^{(j)} &= -\alpha_1^{(j-1)}\beta_p
\end{aligned}
\end{array}
\tag{23}
$$

In order for future outputs to be predicted using the finite difference model, the controlling inputs are applied only over a finite time-span, beyond which the inputs are said to be zero. The cost function to be minimized in the GPC method is defined as

$$
J(k) = \frac{1}{2}\left\{[\mathbf{y}_s(k) - \tilde{\mathbf{y}}_s(k)]^T [\mathbf{y}_s(k) - \tilde{\mathbf{y}}_s(k)] + \mathbf{u}_s^T(k)\Lambda\mathbf{u}_s^T(k)\right\} \tag{24}
$$

where Λ is a diagonal matrix of weighting penalty terms. The term $\tilde{\mathbf{y}}_s$ is the desired vector of future outputs. Optimizing Eq. (24) with respect to $\mathbf{u}_s(k)$ produces

$$
\frac{\partial J(k)}{\partial \mathbf{u}_s(k)} = \left[\frac{\partial \mathbf{y}_s(k)}{\partial \mathbf{u}_s(k)}\right]^T [\mathbf{y}_s(k) - \tilde{\mathbf{y}}_s(k)] + \Lambda\mathbf{u}_s(k) = 0 \tag{25}
$$

where

$$
\frac{\partial \mathbf{y}_s(k)}{\partial \mathbf{u}_s(k)} = \begin{bmatrix}
\dfrac{\partial \mathbf{y}(k)}{\partial \mathbf{u}(k)} & \dfrac{\partial \mathbf{y}(k)}{\partial \mathbf{u}(k+1)} & \cdots & \dfrac{\partial \mathbf{y}(k)}{\partial \mathbf{u}(k+s-1)} \\
\dfrac{\partial \mathbf{y}(k+1)}{\partial \mathbf{u}(k)} & \dfrac{\partial \mathbf{y}(k+1)}{\partial \mathbf{u}(k+1)} & \cdots & \dfrac{\partial \mathbf{y}(k+1)}{\partial \mathbf{u}(k+s-1)} \\
\vdots & \vdots & \ddots & \vdots \\
\dfrac{\partial \mathbf{y}(k+s-1)}{\partial \mathbf{u}(k)} & \dfrac{\partial \mathbf{y}(k+s-1)}{\partial \mathbf{u}(k+1)} & \cdots & \dfrac{\partial \mathbf{y}(k+s-1)}{\partial \mathbf{u}(k+s-1)}
\end{bmatrix} \tag{26}
$$

The general control sequence to be applied to the system over some carefully predetermined control horizon, h_c, is synthesized from introducing Eqs. (19) and (26) into Eq. (25):

$$
\mathbf{u}_s(k) = -\left[(\mathcal{T}^T\mathcal{T} + \Lambda I)^{-1}\mathcal{T}^T\right][\mathcal{B}\mathbf{u}_p(k-p) - \mathcal{A}\mathbf{y}_p(k-p) - \tilde{\mathbf{y}}_s(k)] \tag{27}
$$

where I is a properly-sized identity matrix. The control inputs $\mathbf{u}_s(k)$ are calculated for each time-step as a weighted sum of input and output data back to time-step $k-p$. In the relation in Eq. (27) the first r_c values of the resolved control sequence are collected, the rest are discarded, and a new control vector is synthesized for the next time step.

For the regulation problem

$$
\begin{aligned}
\mathbf{u}(k) &= \text{the first } r \text{ rows of } \left[-(\mathcal{T}^T\mathcal{T} + \Lambda I)^{-1}\mathcal{T}^T\right] \\
&\quad \times [\mathcal{B}\mathbf{u}_p(k-p) - \mathcal{A}\mathbf{y}_p(k-p)] \\
&= \alpha_1^c\mathbf{y}(k-1) + \alpha_2^c\mathbf{y}(k-2) + \cdots + \alpha_p^c\mathbf{y}(k-p) \\
&\quad + \beta_1^c\mathbf{u}(k-1) + \beta_2^c\mathbf{u}(k-2) + \cdots + \beta_p^c\mathbf{u}(k-p)
\end{aligned} \tag{28}
$$

where

$$
\begin{aligned}
\begin{bmatrix}\alpha_1^c & \alpha_2^c & \cdots & \alpha_p^c\end{bmatrix} &= \text{the first } r \text{ rows of } \left[(\mathcal{T}^T\mathcal{T} + \Lambda I)^{-1}\mathcal{T}^T\right]\mathcal{A} \\
\begin{bmatrix}\beta_1^c & \beta_2^c & \cdots & \beta_p^c\end{bmatrix} &= \text{the first } r \text{ rows of } \left[-(\mathcal{T}^T\mathcal{T} + \Lambda I)^{-1}\mathcal{T}^T\right]\mathcal{B}
\end{aligned} \tag{29}
$$

It is important to note that, in Eq. (27), the matrix inverse of $(\mathcal{T}^T\mathcal{T} + \Lambda I)$ for $\Lambda = 0_{r_c \times r_c}$ exists only when the prediction horizon is large enough so that the Toeplitz matrix $\mathcal{T}$ is full rank.

Control Application

According to the proposed system specifications for the HELIOS mission, the heliogyro blades will be monitored using a dedicated camera assembly positioned above the plane of rotation by a deployable mast, seen in Figure 8. Videogrammetry techniques will be applied on the obtained images from the cameras in order to measure deflections at one or several points along each of the blades. Furthermore, a set of dedicated motors are to be housed at the root of each of the blades in order to provide pitch actuation according to some desired maneuver profile.

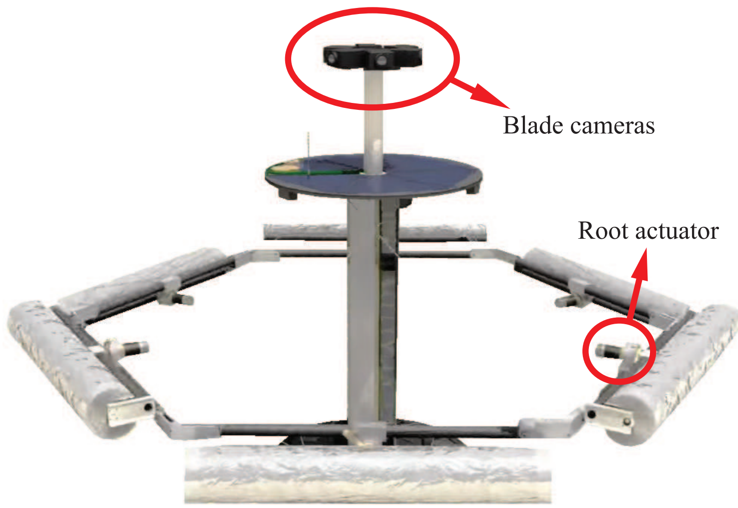

Figure 8: HELIOS Blade Camera on Deployed Mast

In essence, the goal of the controller is twofold: first, it must work to maintain as much blade flatness as possible and, second, it must actuate the blade root to follow prescribed pitching maneuvers. For the sake of simplicity, the root actuator assembly considered in this study is limited to a basic DC motor affixed to the hub structure at its base, and capable of torsional inputs to drive one blade from the root. The gear ratio between the motor shaft and the blade root coupler is assumed to be high enough to prevent back-driving, and sufficiently low to adapt to quickly-changing torsional commands. The DC motor is assumed to have position encoding capability, which allows to monitor the angular position of the driving shaft (θ) for control design purposes. For the sake of space, this paper omits the straightforward design of a simple full state feedback controller on the root motor in order to demonstrate that the root actuator can be designed to track the desired pitching profiles, θ_p.

A set of pitching profiles are applied in coordination to each blade to obtain the desired translational forces or rotational moments about the body axes. To this end, combinations of cyclic, collective, and half-pitch maneuvers are integrated together using a well-known relation for helicopter rotor pitching [6]:

$$\theta_p = \theta_{cy} \sin\left[\omega_p(t - t_0) + \psi_b - \psi\right] + \theta_{hp} \sin\left\{\frac{1}{2}\left[\omega_p(t - t_0) - \frac{\pi}{2} + \psi_b - \psi\right]\right\} + \theta_{co} \tag{30}$$

where ω_p is the pitching angular rate; ψ_b is the phase shift for the ith blade location, and equals $\frac{2\pi}{n_b}(i-1)$; t_0 is the maneuver's initial time; ψ represents a phase shift; while θ_{cy}, θ_{hp}, and θ_{co} are the cyclic, half-pitch, and collective amplitudes, respectively. Therefore, the gist of the control strategy is that the controller is designed to accept desired forces and/or moments (see Figure 1), and the algorithm then provides the appropriate amount of θ_{co}, θ_{cy}, and θ_{hp} profiles to achieve a maneuver which yields the desired dynamics. To be specific, the cyclic maneuver sets all blades to follow a sinusoidal pitching trajectory, which produces a slewing force perpendicular to the plane of the heliogyro. The collective profile alone yields a spin-up or spin-down moment along the rotational axis of the heliogyro structure where all the blades are pitched simultaneously to the same angle. Finally, half-pitching is particularly useful for changing the attitude of the spacecraft, as it produces a moment along a lateral body axis with the blades following a sinusoidal pattern scaled over two revolutions.

When the GPC algorithm is implemented, one of the most important responsibilities of the control engineer is to select the appropriate size for the control horizon parameter p. The size of this variable essentially dictates the amount of dynamic effects that are captured by the identification portion of the GPC procedure, thus ensuring that said effects are ameliorated when the future control histories are synthesized. This is evident when comparing Figures 9a and 9b, which depict a time history of the tip deformations for the two-bladed heliogyro with and without control effort under near-Earth SRP levels and a nominal spin rate, ω_0, of 1 rpm. For these examples, the controller is driven to regulation, that is, to drive the pitching at the tip of the sail to zero over time. A random excitation is given to the system initially in order to 'awaken' its vibrational modes, which is turned off when the GPC starts, $k = 0$, and taken over by the synthesized control inputs. The blue dashed lines represent the free response of the system at $k = 0$.

As the figures show, when implementing GPC on the heliogyro blades, it is desirable to increase the value of p in order to more effectively regulate the vibrations of the system. In fact, it is desirable to set p to be much larger than $\frac{n}{m}$ in order to provide better output predictions, and maintain control for longer after the GPC is turned on.

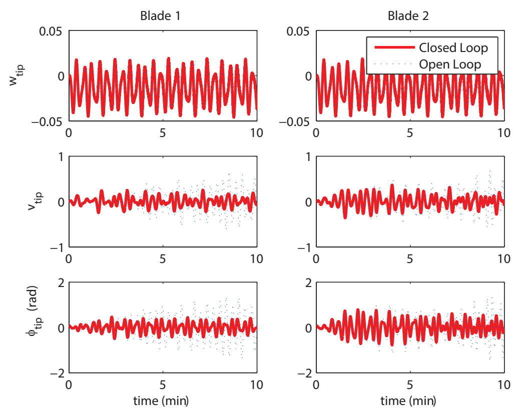

(a) $p = 10$

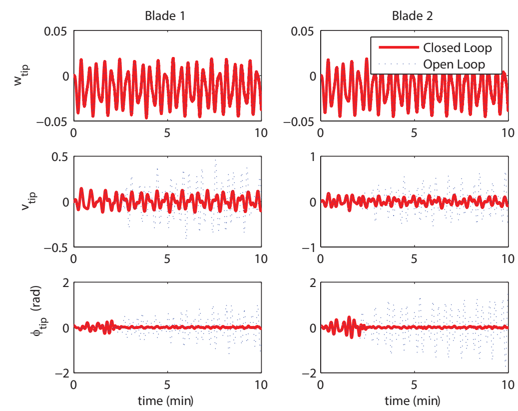

(b) $p = 60$

Figure 9: Tip Angles, GPC Regulation

A time history of the deformations at the tip of the sails does not tell the whole story, since the true goal of the predictive controller is to maintain tautness in the blade so that the SRP vector is uniform along the entire sail. Figure 10 investigates how using different sensor setups can enable the achievement of this goal. In the figure, the left column examines the aforementioned sensor layout of a pair of targets located at the sail tip to be tracked by the hub video camera, while the right column shows results for an additional pair of targets located mid-length along the blade, which is a completely plausible situation given that sufficient computing power is available to handle the new data. In all plots, the green dotted line represents the twisting amplitude of the first segment, the blue dash-dot curve stands for the twisting halfway along the sail, while the red dashed line shows the twisting at the very tip of the blade. These simulations are carried out for a two-bladed vehicle in near-Earth orbital conditions (9.1×10^{-6} Pa of SRP) and a nominal spin rate, ω_0, of 1 rpm, but the results are independent of the sail configuration of the vehicle. It is evident that the second sensor layout, which adds a pair of tracking targets halfway along the blade, performs better at maintaining uniformity than the first layout. However, because the controller is now asked to attend to one additional set of states, this means that the ARX order, p, and the prediction and control horizons must all increase in order to effectively regulate the new system. Conversely, for the standard measurement layout, Figures 10c and 10e show the controller to be sluggish in achieving the goal of regulation, yet less demanding of measurement data (p size) to identify the dynamic model. A change in the control weighting matrix, Λ, does not offer a discernible alteration in performance.

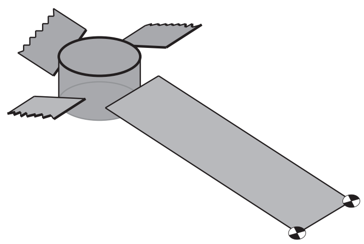

(a) Sensor Layout # 1

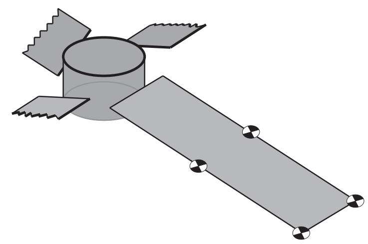

(b) Sensor Layout # 2

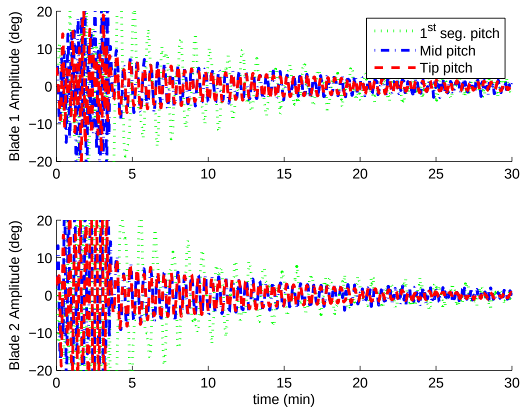

(c) Layout # 1 ($p = 200$, $\lambda = 100$)

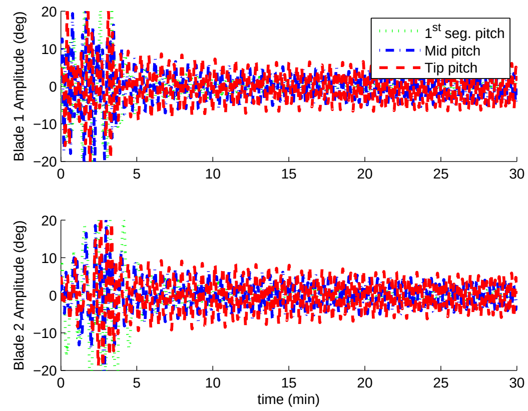

(d) Layout # 2 ($p = 200$, $\lambda = 1000$)

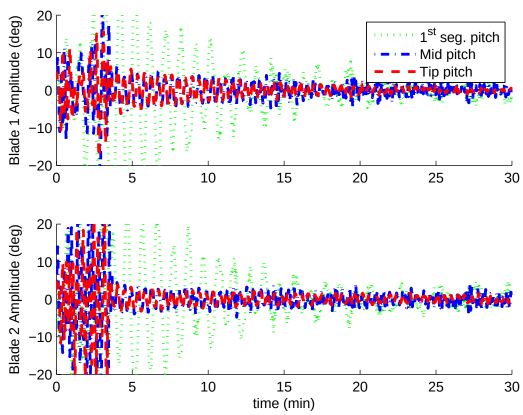

(e) Layout # 1 ($p = 200$, $\lambda = 1000$)

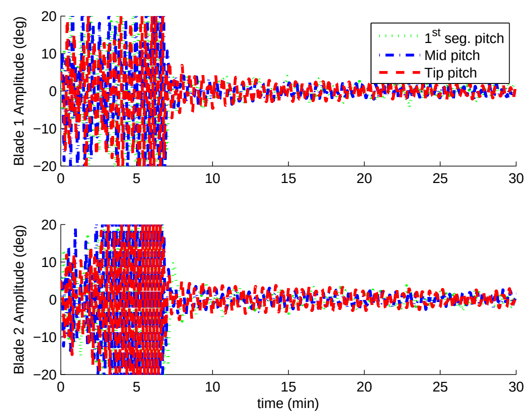

(f) Layout # 2 ($p = 400$, $\lambda = 1000$)

Figure 10: Blade Uniformity Results from Differing Sensor Layouts

Figure 11 depicts the pitching (in degrees) at various stations along a blade with respect to the desired cyclic maneuver imposed at the root (black curve). The plot shows the dynamics of the system right after the GPC action is turned on –at about the 3-minute mark, in this instance. The controller is shown to effectively induce the sail to follow the desired profile. Some lag in command from the imposed maneuver at the root to the tip response is seen to eventually abate. When a certain pitching is desired, the blade is forced to converge onto dynamics which may clash with the dynamics of the heliogyro system itself. This is why it is desirable to scale the frequency of the pitching maneuvers, ω_p in Eq. 30, to be a multiple of the spin rate, ω_0, of the heliogyro, which is a frequency that the blades are naturally disposed to follow. Aside from the fact that this strategy is necessary to effectively conduct cyclic or half-pitch maneuvers, it also conserves energy at the actuator mechanism and prevents the awakening of high-frequency uncontrollable modes.

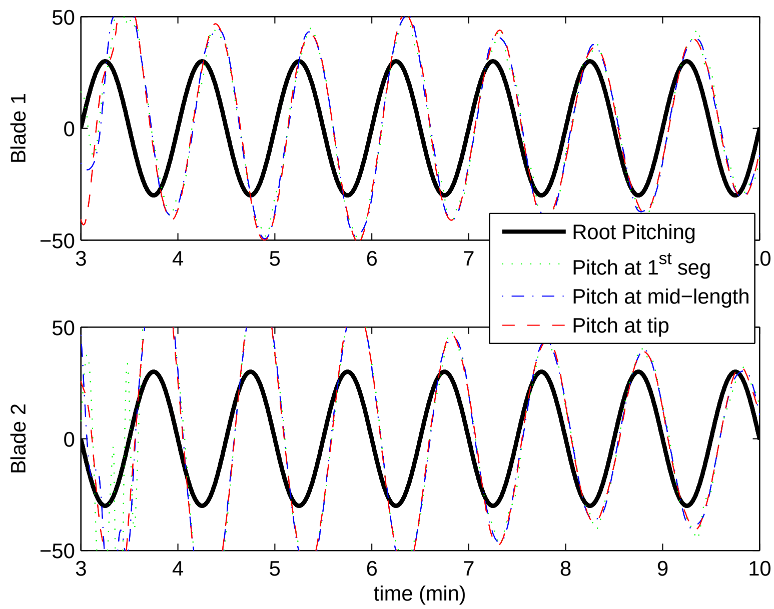

Figure 11: Pitching Along the Blade, $\theta_{cy} = 30°$

Conclusions

This paper introduces a modeling method which formulates an individual sail of a heliogyro as a series of lumped masses connected by rigid massless rods. The technique is designed to preserve important coupling effects between the heliogyro blade vibrations, which is itself an improvement over a significant part of past literature. An essential aspect of the lumped-mass approximation philosophy is the interpretation of the heliogyro blade as the special case of a very thin helicopter rotor. To this end, the strain-displacement relations which are usually associated with helicopter rotor theory are utilized to derive aeroelastic effects which are assimilated into the lumped-mass model via energy formulations.

The occurrence of flutter instabilities, caused by the coupling between the in-plane and twisting modes of the system, is predicted at certain orbital conditions. The prediction of the flutter phenomenon is important to the eventual design of heliogyro mission trajectories, and in the sense that it is a property which can be reproduced with an arguably simple modeling procedure such as the lumped-mass approach. Studies conducted using a predictive control algorithm demonstrate that it is possible to achieve a reasonable amount of blade uniformity (to within 5 degrees of amplitude all along the blade) and follow pitching commands using generalized predictive control (GPC). Care must be taken when designing the control and system identification parameters of GPC in order to capture the necessary data under varying orbital conditions.

References

[1]McInnes, C., *Solar Sailing: Technology, Dynamics and Mission Applications*, Springer Science & Business Media, 2013.

[2]MacNeal, R., *The Heliogyro: An Interplanetary Flying Machine*, NASA Contractor Report CR 84460, 1967.

[3]Hodges, D. and Dowell, E., *Nonlinear Equation of Motion for the Elastic Bending and Torsion of Twisting Nonuniform Rotor Blades*, NASA Technical Note D-7818, 1974.

[4]MacNeal, R., *Structural Dynamics of the Heliogyro*, NASA Contractor Report CR 1745A, 1971.

[5]Natori, M., Nemat-Nasser, S., and Mitsugi, J., "Instabiliy of a Rotating Blade Subjected to Solar Radiation Pressure," *AIAA Structure, Structural Dynamics, and Materials Conference*, April 1989.

[6]Blomquist, R., *Heliogyro Control*, Ph.D. Dissertation, The Robotics Institute, Carnegie Mellon University, 2009.

[7]Juang, J., Hung, C., and Wilkie, K., "Dynamics of a Spinning Membrane," *AAS Jer-Nan Juang Astrodynamics Symposium. Paper 2012-601*, College Station, TX, June 2012.

[8]Huang, Y., Juang, J., Hung, C., and Wilkie, K., "Dynamics of a Coupled Pendulum Model of a Heliogyro Membrane Blade," *3rd Int'l Symposium on Solar Sailing*, Glasgow, UK., June 2012.

[9]Tsai, L., Pimienta-Peñalver, A., Crassidis, J., and Juang, J., "Dynamics of a Spinning Structure Subjected to Uniform Pressure," *6th International Conference on High Performance Scientific Computing. Paper 31*, Hanoi, Vietnam, March 2015.

[10]Guerrant, D., Lawrence, D., and Wilkie, K., "Heliogyro Solar Sail Blade Twist Control," *35th Annual AAS Guidance and Control Conference*, Breckenridge, CO, February 2012.

[11]Wilkie, W., Warren, J., Horta, L., Lyle, K., Juang, J., Littell, J., Bryant, R., Thomson, M., Walkemeyer, P., Guerrant, D., Lawrence, D., Gibbs, S., Dowell, E., and Heaton, A., "Heliogyro Solar Sail Research at NASA," *Advances in Solar Sailing*, Springer, 2014, pp. 631–650.

[12]Tsai, L., *Stability Analysis and Dynamic Response of a Membrane Blade of Heliogyro Solar Sail*, M.S. Thesis. Department of Engineering Science, National Cheng Kung University, Tainan City, Taiwan., 2016.

[13]Meirovitch, R., "Hybrid state equations of motion for flexible bodies in terms of quasi-coordinates," *Journal of Guidance, Control, and Dynamics*, Vol. 14, 1991, pp. 1008–1013.

[14]Pimienta-Peñalver, A., Tsai, L., Juang, J., and Crassidis, J., "Attitude Dynamics and Stability Analysis of a Heliogyro Solar Sail," *4th International Symposium on Solar Sailing. Paper 17058*, Kyoto, Japan, January 2017.

[15]Juang, J., Warren, J., Horta, L., and W.K., W., "Progress in NASA Heliogyro Solar Sail Structural Dynamics and Solarelastic Stability Research," *4th International Symposium on Solar Sailing. Paper 17080*, Kyoto, Japan, January 2017.

[16]Juang, J. and Phan, M., *Identification and Control of Mechanical Systems*, Cambridge University Press, 2001.